

Article

Effect of Primary γ' Phase on High-Temperature Endurance Performance of GH4720Li Superalloy

Xing Zhou ¹, Ruifeng Dong ^{1,*} , Yuchang Xie ¹, Shuoqi Hu ¹, Tianyuan Xu ¹, Jian Li ¹ and Wei Zhang ²

¹ College of Materials Science and Engineering, Inner Mongolia University of Technology, Hohhot 010051, China; 15541555629@163.com (X.Z.); 18135162874@163.com (Y.X.); hushuoqi7@163.com (S.H.); xty13180807835@163.com (T.X.); 15144708423@163.com (J.L.)

² School of Materials Science and Engineering, Nanjing University of Science and Technology, Nanjing 210094, China; zwei3203@163.com

* Correspondence: drfcsp@163.com or drfcsp@imut.edu.cn

Abstract: To investigate the effect of the primary γ' phase on the high-temperature endurance performance of GH4720Li superalloy, samples with different volume fractions of the primary γ' phase were prepared by adjusting the heat treatment process. The high-temperature endurance performance was tested, and the microstructure was examined. Results indicate that samples with a higher volume fraction of the γ' phase exhibit a greater stress rupture life. Additionally, alloy samples with varying γ' phase volume fractions show improved plasticity and toughness at 760 °C/530 MPa. Fracture morphology results reveal that high-volume-fraction primary γ' phase samples primarily undergo transgranular fracture, whereas low-volume-fraction samples exhibit intergranular fracture due to grain boundary sliding. During high-temperature endurance, the secondary γ' phase in the crystal is affected. Long-term aging refines the secondary γ' phase, resulting in a more uniform distribution. Finally, the influence of the primary γ' phase and the creep behavior of each material group on high-temperature endurance performance are discussed.

Keywords: GH4720Li; high-temperature endurance performance; primary γ' phase



Citation: Zhou, X.; Dong, R.; Xie, Y.; Hu, S.; Xu, T.; Li, J.; Zhang, W. Effect of Primary γ' Phase on High-Temperature Endurance Performance of GH4720Li Superalloy. *Crystals* **2024**, *14*, 851. <https://doi.org/10.3390/cryst14100851>

Academic Editors: Marzena Lachowicz and Erdem Karakulak

Received: 5 September 2024
Revised: 23 September 2024
Accepted: 27 September 2024
Published: 28 September 2024



Copyright: © 2024 by the authors. Licensee MDPI, Basel, Switzerland. This article is an open access article distributed under the terms and conditions of the Creative Commons Attribution (CC BY) license (<https://creativecommons.org/licenses/by/4.0/>).

1. Introduction

GH4720Li alloy is a nickel-based aging strengthened superalloy with high service temperature and high-temperature strength. It is mainly used to manufacture aero-engine turbine disks with a service temperature of 650–750 °C. It has excellent properties such as high strength, corrosion resistance, oxidation resistance, and fatigue resistance [1–4]. The main strengthening phase of GH4720Li is the γ' phase with a content of up to 40% [5,6], including the primary γ' phase (1–10 μm) at grain boundaries, secondary γ' phase (90–300 nm) in grains, and dispersed tertiary γ' phase (15–60 nm).

The γ' phase, typically consisting of Ni₃(Al, Ti), is a coherent, intermetallic precipitate that plays a crucial role in strengthening nickel-based superalloys [7,8]. It imparts high-temperature strength and creep resistance by impeding dislocation motion during deformation [9–11]. The size, distribution, and morphology of γ' precipitates are critical factors that determine the overall mechanical properties of superalloys [12–16]. Consequently, controlling and optimizing the γ' phase through various processing techniques, particularly heat treatment, has been a focal point in materials engineering research.

Heat treatment is a fundamental process employed to tailor the microstructure and, hence, the mechanical properties of superalloys. Previous studies have demonstrated that high-temperature solution treatments can dissolve coarse γ' precipitates and homogenize the alloy's composition. By manipulating parameters such as temperature, cooling rate, and holding time, it is possible to control the dissolution nucleation, growth, and distribution of the γ' phase within the alloy matrix [9,10,12,17]. Zhang [18] obtained the correlation between the heat treatment process and γ' phase morphology by adjusting the temperature

and time of solid solution and aging. Song [19] found that the size and distribution of three kinds of γ' phases were affected by different solution temperatures under the same aging system. Tang [20] found that the grains of GH4720Li alloy without a primary γ' phase grew abnormally, and the properties of the material decreased sharply without the pinning effect of the γ' phase on the grain boundary. Zhang [21] found that the precipitated γ' phase plays an active role in the creep process of superalloys. Tsai [22] found that the refined γ' phase can increase the thermal stability of the material during creep in the creep test of fine-grained nickel-based superalloys. Zhang [23], in the long-term aging test of In617, found that the γ' phase coarsens during long-term aging, and a new heat treatment process was proposed to prevent the coarsening of the γ' phase.

Current research on GH4720Li superalloy primarily explores the relationship between individual mechanical properties and microstructure, with a particular emphasis on the influence of intragranular precipitates on performance. However, the effect of primary γ' precipitates at grain boundaries on high-temperature properties is rarely studied. To investigate the effect of primary γ' on rupture life, two samples with identical grain size but different volume fractions of the primary γ' phase were prepared by modifying the heat treatment process. High-temperature endurance tests were conducted at 680 °C/830 MPa and 730 °C/530 MPa, respectively. The influence of different primary γ' phases on high-temperature performance was examined, along with an analysis of the transformation process and creep mechanism of the γ' phase during high-temperature endurance. This research offers theoretical support for developing high-performance turbine disks.

2. Material and Experimental Procedures

The experimental material GH4720Li superalloy is taken from the turbine disk forging, and the nominal chemical composition (wt%) of GH4720Li investigated in the present work is as follows: 15.79 Cr, 14.68 Co, 0.14 Fe, 4.92 Ti, 2.59 Al, 2.97 Mo and Ni balance. The original microstructure of GH4720Li alloy and the XRD phase analysis of the main phases are shown in Figure 1. The main phase in the matrix is γ' -AlNi₃.

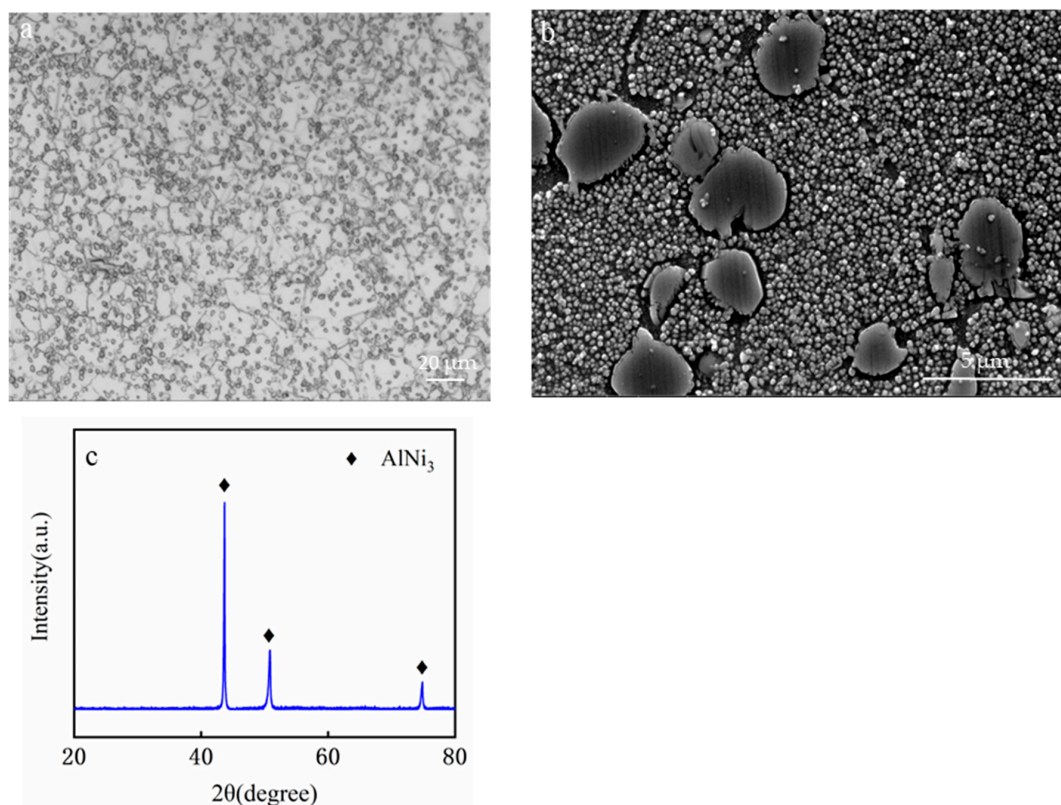


Figure 1. Original microstructure of GH4720Li alloy; (a) OM, (b) SEM, (c) XRD.

In order to obtain the microstructure with the same grain size and different primary γ' phase morphology, two different solid solution treatment processes were carried out on the disk forgings. The solid solution treatment process is shown in Figure 2. The same $650\text{ }^{\circ}\text{C} \times 24\text{ h} + 760\text{ }^{\circ}\text{C} \times 16\text{ h}$ bipolar aging treatment was adopted for the two forgings after solid solution, and the aging treatment was air-cooled.

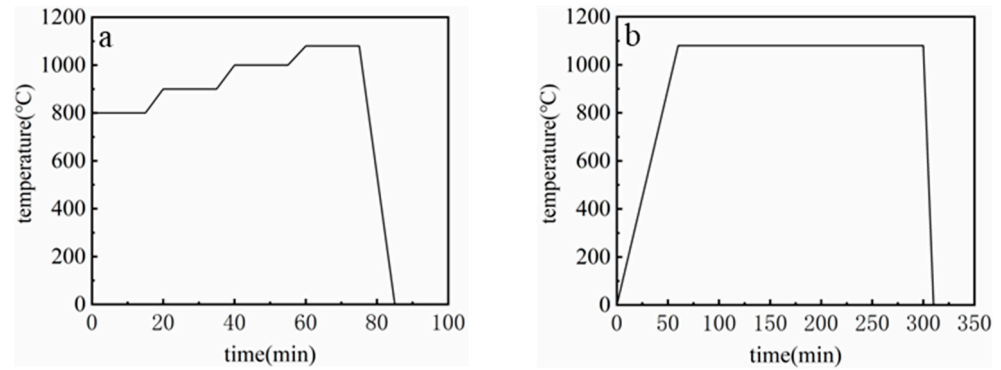


Figure 2. Solution treatment process; (a) gradient process, (b) standard process.

The plate forgings after heat treatment were sampled at 1/4 of the diameter, and the microstructure observation and high-temperature endurance performance test were carried out. The intragranular γ' phase was observed and photographed by an FEI 650 scanning electron microscope, and precipitated phase electrolytic corrosion was carried out in 170 mL H_3PO_4 , 10 mL H_2SO_4 , and 15 g CrO_3 solution. Electrolytic corrosion was performed using DC voltage 5 V, current 1~2.5 A, and time 5~12 s. The size of the γ' phase was statistically analyzed by fiji Image J v1.53q software. The high-temperature endurance test and sample size were carried out according to GB/T 2039-2012 Metallic material–uniaxial creep testing method in tension, and the sample size and shape are shown in Figure 3. The temperature stress conditions of the high-temperature endurance test are $730\text{ }^{\circ}\text{C}/530\text{ MPa}$ and $680\text{ }^{\circ}\text{C}/830\text{ MPa}$. The fracture morphology was observed and photographed by an FEI 650 scanning electron microscope, and the microstructure after fracture was observed by sampling at 1.5 mm parallel to the fracture. The γ' phase after the high-temperature endurance experiment was observed by an FEI 650 scanning electron microscope. The grain orientation and plastic deformation near the rupture fracture were analyzed by electron backscatter diffraction (EBSD). The electrolytic polishing electrolyte is 20 mL H_2SO_4 and 80 mL CH_3OH . The electrolytic process parameters are DC voltage 25 V, current 1~1.5 A, and time 5~12 s.

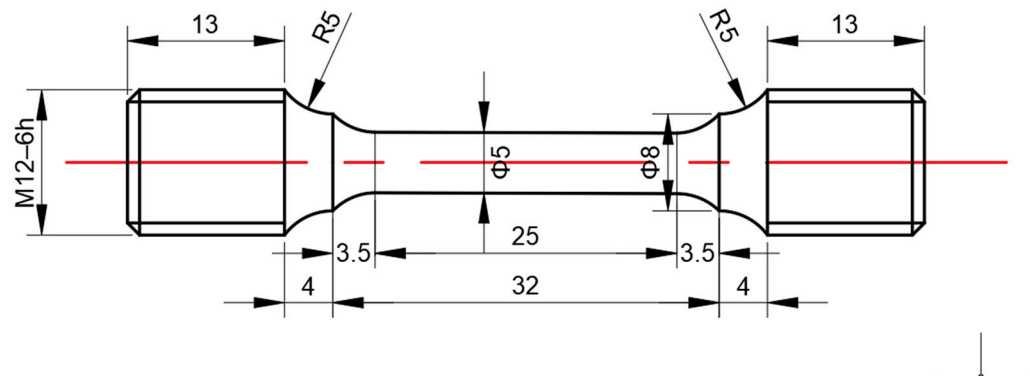


Figure 3. Size of high-temperature endurance performance sample.

3. Results

3.1. Effects of Different Heat Treatment Processes on γ' Phase

The microstructure of GH4720Li superalloy after different heat treatment processes is displayed in Figure 4. The size and quantity of the primary γ' phase at the grain boundary vary significantly. In the gradient heating process, a large number of larger primary γ' phases remain at the grain boundary. In the standard heat treatment, the primary γ' phase at the grain boundary dissolves significantly and is smaller in size, but the grain sizes of the samples under both processes are similar. The average grain size in Figure 4a is 17.15 μm , while in Figure 4b, it is 17.05 μm . The primary γ' phase at the grain boundary inhibits grain boundary migration and restricts grain growth by pinning the boundary. During the solid solution process, the primary γ' phase at the grain boundary gradually dissolves as the holding time increases. After the gradient process, the average particle size of the primary γ' phase is 5.01 μm , with a volume fraction of 17.90%. Under the standard heat treatment, the primary γ' phase has an average size of 4.03 μm and a volume fraction of 14.15% (Figure 5). Despite the dissolution, the residual primary γ' phase still pins the grain boundary, preventing grain growth, which results in similar grain sizes between the two processes.

Before heat treatment, the secondary γ' phase within the crystal is irregular in shape (Figure 1b), uniformly distributed in the matrix with an average size of 145 nm, and no tertiary γ' phase is observed. After heat treatment, the crystal contains two main types of γ' phases: the coarsened secondary γ' phase and the nanoscale tertiary γ' phase. The number of secondary γ' phases is significantly reduced, while their size increases compared to pre-heat treatment. The secondary γ' phase measures 246 nm after the gradient heating process and 262 nm after the standard process. The tertiary γ' phase is dispersed throughout the matrix.

The melting temperature of the γ' phase in GH4720Li superalloy is 1150 $^{\circ}\text{C}$. Based on the Gibbs–Thomson effect, the solubility of the precipitate decreases as its size increases, causing the secondary and tertiary γ' phases in the crystal to dissolve first during the solid solution process. Due to the significant increase in Al and Ti supersaturation during the solid solution process, the secondary γ' phase nucleates at the high-temperature stage of cooling. As the cooling process is brief, the amount of secondary γ' phase in the matrix is limited. In this experiment, without a controlled cooling rate, the morphology of the secondary γ' phases in both heat treatment processes remains similar. Despite secondary γ' phase nucleation during cooling, the matrix remains supersaturated with alloying elements, leading to tertiary γ' phase nucleation during aging. During aging, the secondary γ' phase coarsens, and after reaching a certain size, dissolves into the γ matrix, promoting further nucleation of the tertiary γ' phase. Thus, the secondary γ' phase observed in Figure 6 is coarsened during aging, with Al and Ti atoms for tertiary phase nucleation coming from two sources. One source is the dissolution of secondary γ' and primary phases during solid solution, while the other is the dissolution of secondary γ' phases during secondary aging.

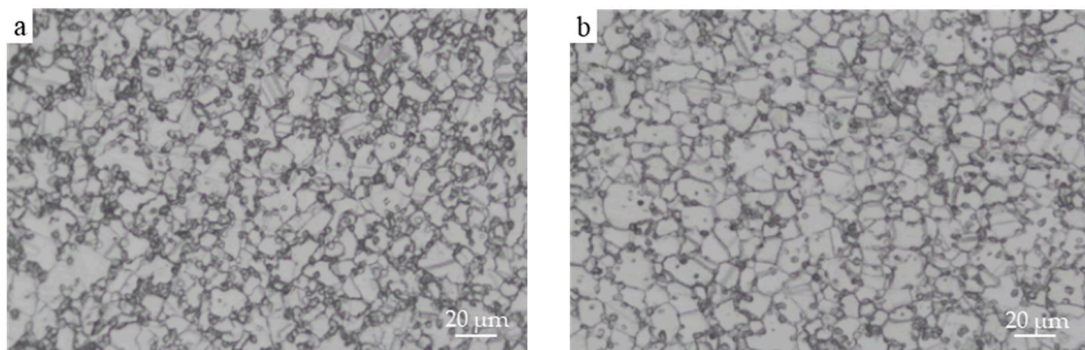


Figure 4. Grain morphology after heat treatment; (a) gradient process, (b) standard process.

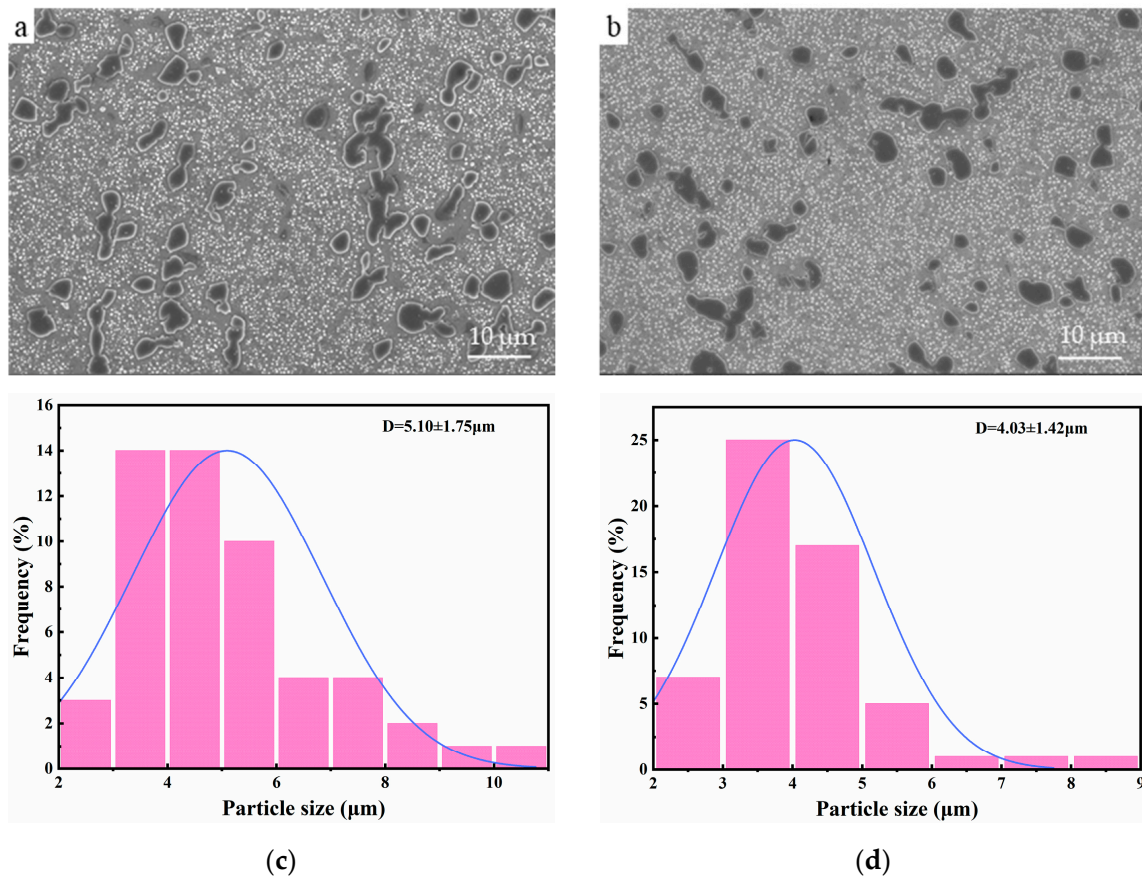


Figure 5. Morphology and size distribution of the primary γ' phase after heat treatment; (a) gradient process, (b) standard process. (c) size of the primary γ' phase of the gradient process (d) size of the primary γ' phase of the standard process.

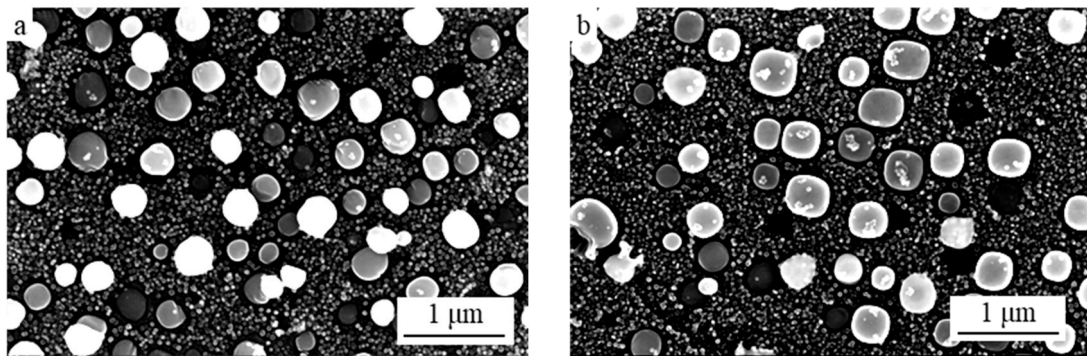


Figure 6. Microstructure of secondary γ' phase after heat treatment; (a) gradient process, (b) standard process.

3.2. High-Temperature Endurance Performance

The high-temperature endurance performance of the samples after different heat treatment processes is shown in Table 1. Through the comparison of multiple sets of data, it can be found that the rupture strength under the gradient heating process is significantly higher than that of the standard process, and the four groups of samples have different degrees of plastic deformation. Among them, the plasticity of group B is the highest, which is 35% A_u , 56% Z_u . Group A has the worst plasticity, which is 12% A_u , 18% Z_u . The plasticity of the material in the endurance test shows that it has higher plasticity at 730 °C/530 MPa.

Table 1. Results of high-temperature endurance performance.

Sample Process	Test Condition	Stress-Rupture Life (t_u), h	Elongation (A_u), %	Shrinkage Rate (Z_u), %	Numbering
Gradient process	680 °C/830 MPa	225	12	18	A
Gradient process	730 °C/530 MPa	125	35	56	B
Standard process	680 °C/830 MPa	71	12	20	C
Standard process	730 °C/530 MPa	65	17	22	D

3.3. Fracture Appearance

Figure 7 is the fracture SEM morphology of group A samples. From the macroscopic fracture (Figure 7a), it can be found that during the endurance test, the crack source is first generated at the I positions, and the crack phase generated by the I position diffuses and grows around. Obvious cleavage lines and a small number of micropores were found in Figure 7b, and the proportion of micropores in the fracture increased with the further growth of the crack (Figure 7c). During the rupture process, the fracture mode changes from quasi-cleavage fracture and micropore aggregation fracture to plastic fracture dominated by micropore aggregation, and the residual primary γ' phase can be obviously observed in the microstructure of the instantaneous fracture zone (Figure 7d). This indicates that the primary γ' phase is the main reason for the generation of micropores during the rupture process.

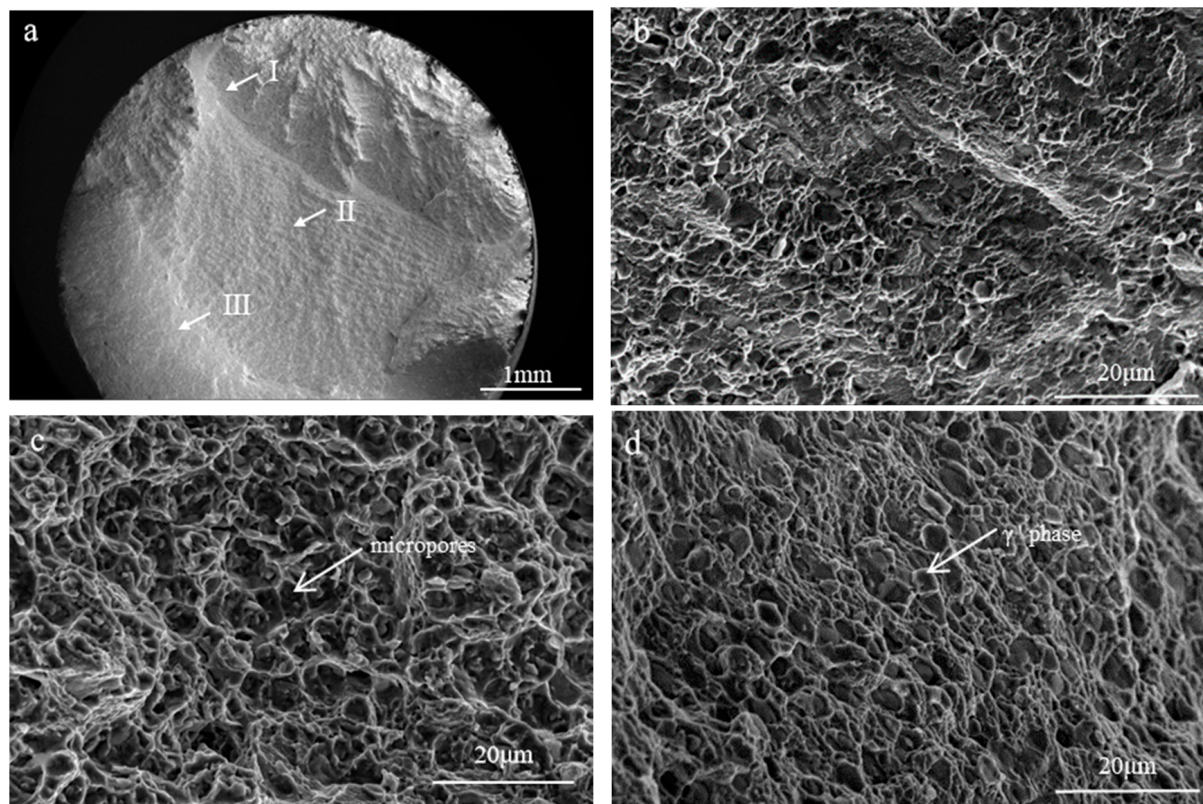


Figure 7. Fracture morphology of group A sample; (a) macroscopic morphology, (b) micro-morphology of point I, (c) micro-morphology of point II, (d) micro-morphology of point III.

Figure 8 is the fracture SEM morphology of group B samples. According to the macroscopic morphology, it can be inferred that the crack first initiates from the I position, the crack grows along the arrow direction during the crack extension, and finally, the instantaneous fracture occurs in the III region. A large number of micropores can be seen in

the crack source and crack growth process, and a small amount of micropores can be found in the instantaneous fracture zone. In the process of forming micropores, instantaneous fracture occurs due to excessive local stress. Combined with the macroscopic morphology of the fracture, the fracture under the test conditions in this group is microporous aggregation ductile fracture.

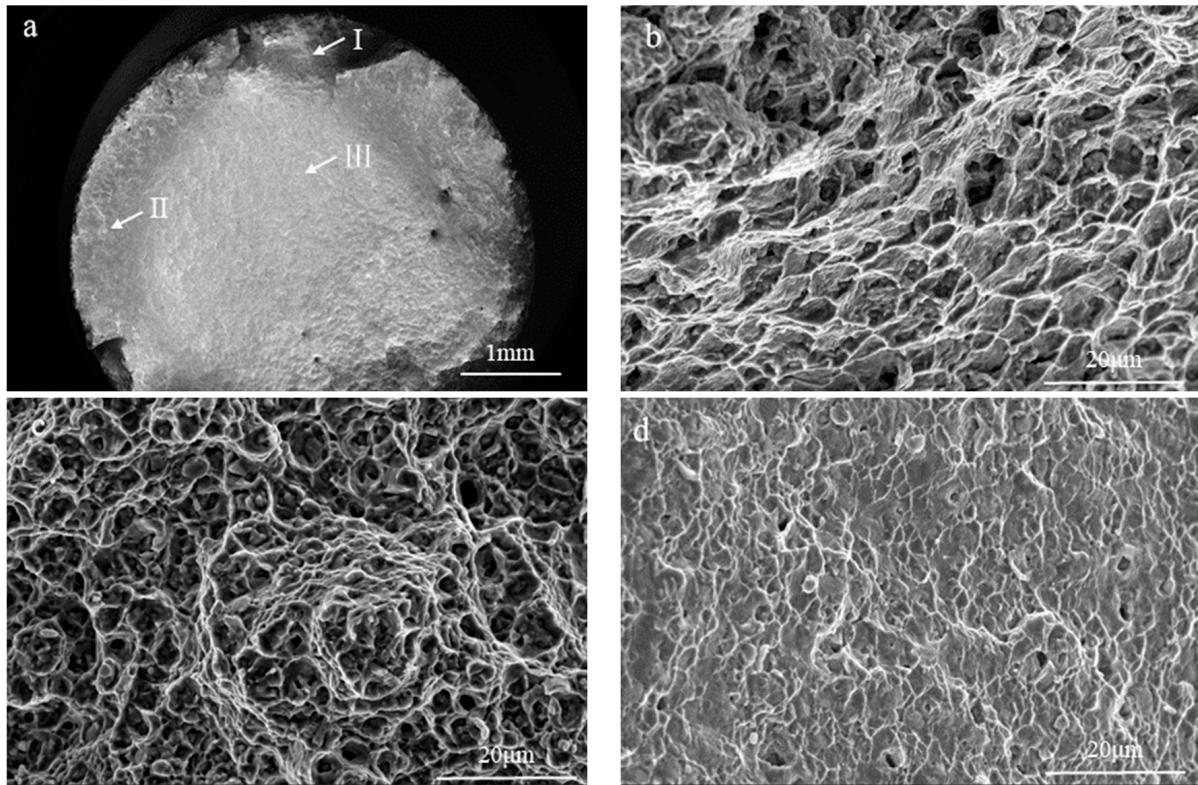


Figure 8. Fracture morphology of group B sample; (a) macroscopic morphology, (b) micro-morphology of point I, (c) micro-morphology of point II, (d) micro-morphology of point III.

Figure 9 is the fracture SEM morphology of group C samples. It can be clearly seen from the macroscopic fracture morphology that the whole fracture morphology consists of three regions: river-like pattern region, smooth region, and shear lip formed by instantaneous fracture. In the river pattern area, the river pattern is obviously developed from point I; that is to say, point a is the position where the crack first occurs. Microscopic characterization of different regions of the fracture shows that the fracture mode of the crack initiation position is mainly quasi-cleavage fracture, and the grain boundary sliding phenomenon is found, but no obvious intergranular fracture is found (Figure 9b). With the growth of cracks, it is found in the SEM image of point II that in addition to cleavage and grain boundary sliding, micropores are generated near the primary γ' phase (Figure 9c), and the fracture mode changes from. This leads to the fact that the fracture morphology at position III is mainly composed of micropores (Figure 9d). In the ESM diagram of the instantaneous fracture zone (Figure 9e), the micropores that are nucleated but not fully grown and not connected to form cracks are found, which proves that the cracks are expanding in the unfractured area in the way of micropore aggregation before the instantaneous fracture of the sample. The fracture mode of the sample in group C is mainly composed of the following three parts. The cleavage fracture and the grain boundary sliding produce the crack source, then the cleavage fracture and the grain boundary sliding change to the micropore aggregation, and finally, the instantaneous fracture is caused by the excessive local stress.

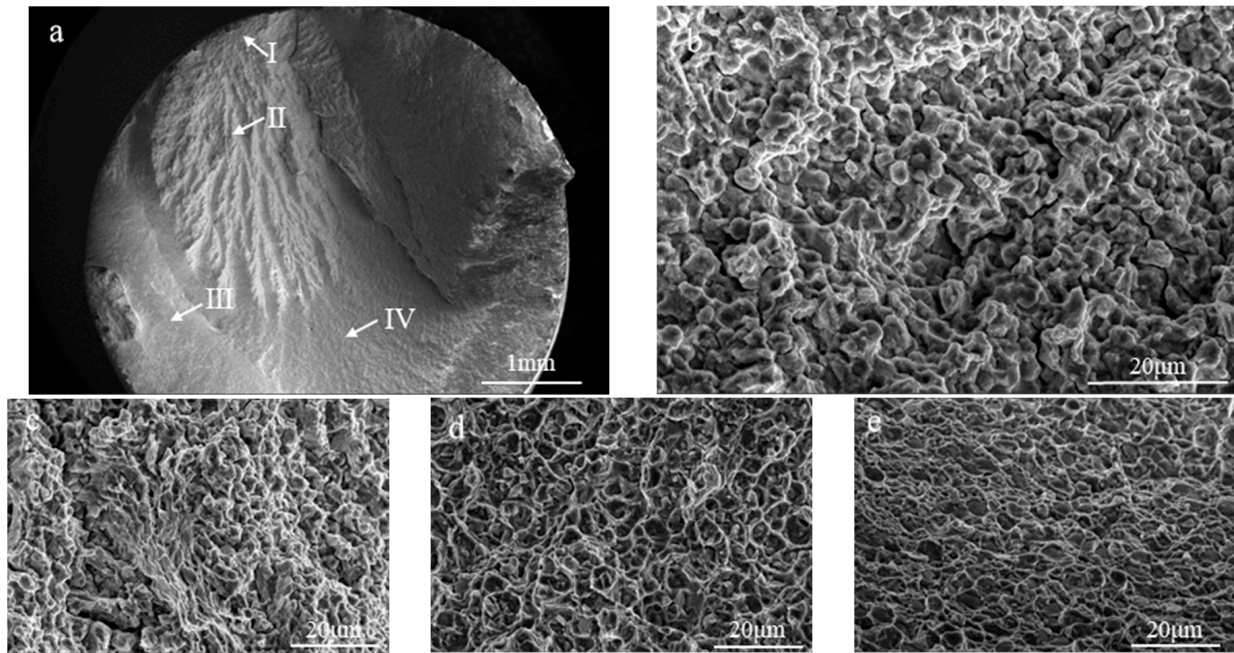


Figure 9. Fracture morphology of group C sample; (a) macroscopic morphology, (b) micro-morphology of point I, (c) micro-morphology of point II, (d) micro-morphology of point III, (e) micro-morphology of point IV.

Figure 10 is the fracture SEM morphology of group D samples. The macroscopic morphology of the fracture is composed of obvious river-like patterns and instantaneous fracture zones. The crack is first generated at point I, and then extends around, and finally breaks. Figure 10b is the microstructure diagram of the crack source, and the block morphology and grain boundary cracks can be clearly seen, indicating that the main fracture mode at the crack source is intergranular fracture caused by grain boundary sliding. With the expansion of the crack, the block morphology disappears, but the cracks along the grain boundary still exist (Figure 10c). The quasi-cleavage fracture characteristics can be clearly seen in the microscopic morphology of the instantaneous fracture zone (Figure 10d). The fracture mode of group D is intergranular fracture initiation crack caused by grain boundary sliding, and the fracture mode changes from intergranular fracture to quasi-cleavage fracture during crack growth.

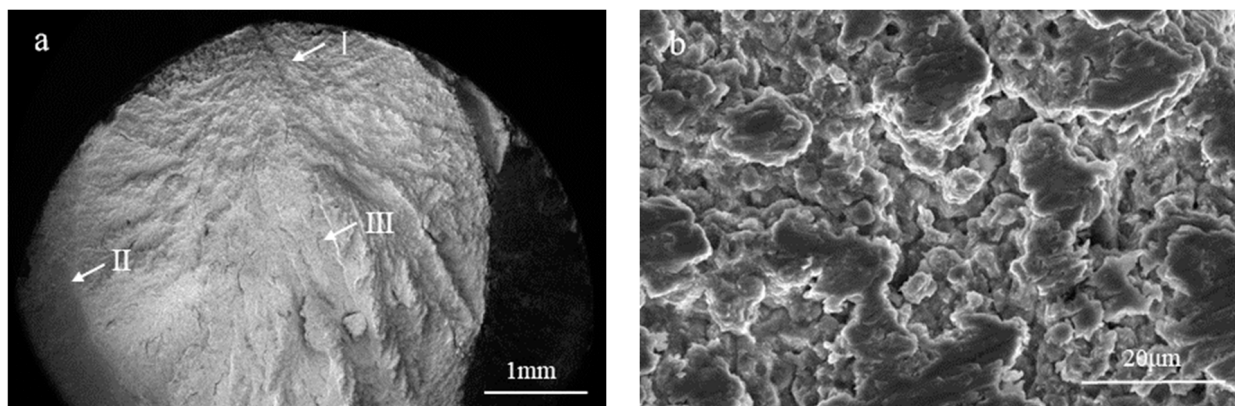


Figure 10. Cont.

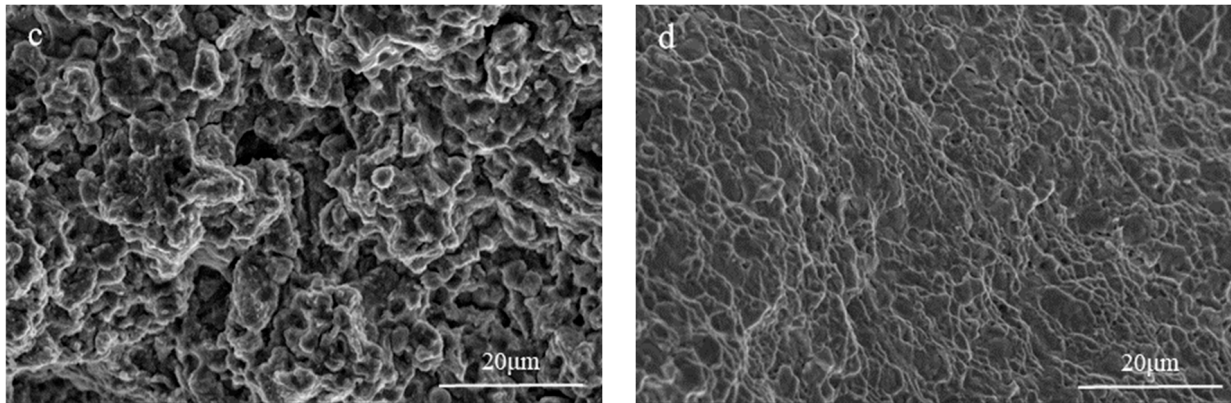


Figure 10. Fracture morphology of group D sample; (a) macroscopic morphology, (b) micro-morphology of point I, (c) micro-morphology of point II, (d) micro-morphology of point III.

3.4. Effect of the High-Temperature Endurance Process on the Secondary γ' Phase

During the high-temperature endurance test, the long-term retention of the sample at the aging temperature of the material has different effects on the γ' phase of the four groups of samples. Figure 11 shows the γ' phase morphology of the four groups of materials after the endurance test. It can be seen that the γ' phase of the four groups of samples has different degrees of dissolution. Through the statistics of the γ' phase of the four groups of samples, it is found that the particle size of the γ' phase of each group of samples decreases before the lasting experiment. The number of γ' phases in both group C and group D decreased significantly. Moreover, the number of γ' phases in group D was the least and the most non-uniform. Considering the rupture life, the more uniform distribution of the γ' phase during the aging process is attributed to the extended aging time. In the long-term aging process of GH4720Li alloy, it is actually a dynamic equilibrium process between the γ matrix and γ' phase in the material. The unstable γ' phase will dissolve in the matrix, and then the supersaturated solute atoms in the matrix will precipitate in the form of the γ' phase. Under the long-term aging effect, the dynamic equilibrium between the γ matrix and γ' phase is achieved.

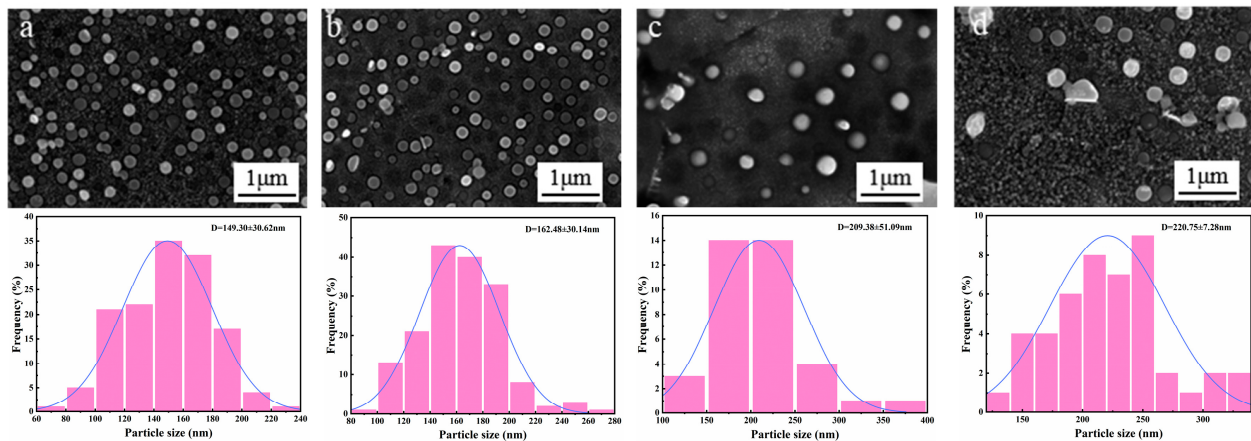


Figure 11. The morphology and size distribution of the secondary γ' phase after high-temperature endurance; (a) group A, (b) group B, (c) group C, (d) group D.

4. Discussion

4.1. Effect of Primary γ' Phase on Endurance Performance

Comparing the rupture life and fracture modes of different groups reveals that the volume fraction of primary γ' significantly affects both rupture life and fracture behavior. Figure 12 shows the EBSD-KAM diagrams of various samples after fracture. Comparing

the KAM diagrams of samples AB and CD shows that the sample with a high-volume fraction of primary γ' phase retains many dislocations, whereas in the low-volume-fraction sample, dislocations are concentrated at the grain boundary, and the KAM value within the grains is lower. At high temperatures, atomic diffusion is enhanced, reducing resistance to dislocation migration. Under constant stress, dislocations steadily migrate toward the grain boundary. The γ' phase is brittle [24,25], preventing plastic deformation and hindering dislocation entry. As a result, dislocations accumulate at the interface between the grain boundary and the primary γ' phase, preventing further migration of dislocations from the crystal to the grain boundary. Compared to the low-volume-fraction primary γ' phase, the high-volume-fraction γ' phase can absorb more dislocations at the phase-matrix interface. In the low-volume-fraction sample, dislocations are more prone to forming microcracks and promoting grain boundary slip.

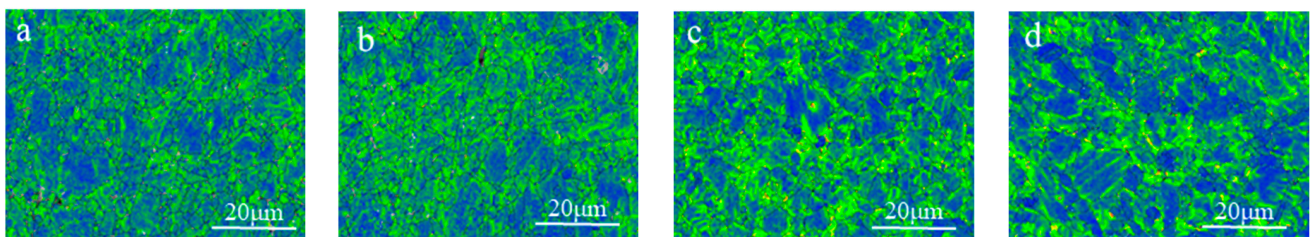


Figure 12. EBSD-KAM diagram of different samples after the fracture; (a) group A, (b) group B, (c) group C, (d) group D.

Additionally, at high temperatures, the intracrystalline strength decreases sharply, leading to transgranular fracture during stress rupture. The fracture mechanism during stress rupture is complex, but the presence of the γ' phase plays a critical role in inhibiting fracture progression. As shown in Figure 13, during transgranular fracture, intragranular cracks propagate under sustained stress. However, the presence of the primary γ' phase prevents rapid crack propagation into macroscopic cracks, instead causing the formation of micropores around the primary γ' phase. These micropores gradually grow and coalesce into larger cracks. In the high-volume-fraction GH4720Li superalloy, grain tearing does not immediately cause material fracture. Fracture in this material is primarily driven by the formation and coalescence of micropores into cracks. In the low-volume-fraction GH4720Li alloy, the scarcity of primary γ' phases offers minimal resistance during transgranular fracture and grain boundary sliding, resulting in a lack of micropore formation and reduced rupture strength.

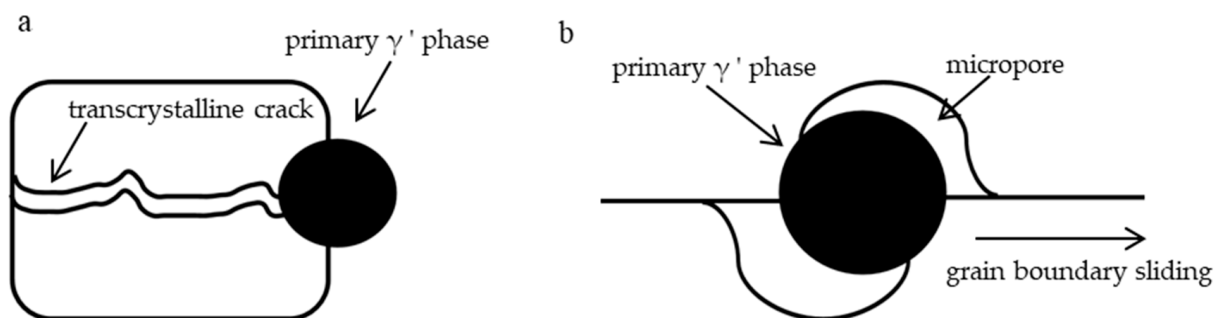


Figure 13. Influence mechanism of primary γ' phase in the fracture process; (a) transcrystalline rupture, (b) grain boundary sliding.

4.2. Creep Behavior in High-Temperature Endurance Process

The creep process of the material can be roughly divided into two stages, namely the steady-state creep stage and the accelerated creep stage. In the steady-state creep process, the creep rate remains unchanged, the hardening and softening are balanced, and the

creep rate in this stage is the smallest. In the accelerated creep process, the strain rate begins to increase with time, and finally leads to unstable fracture. In the steady-state creep process, the atomic motion amplitude at 730 °C is larger than that at 680 °C, the dislocation motion resistance is smaller, and the dislocation slips faster. At 730 °C, the plastic deformation rate is larger during the creep process, but the life is reduced [24,26–28]. The primary γ' phase can hinder the deformation of grains during plastic deformation, so the materials with different primary γ' phases show obvious different life. The creep process of 730 °C/530 MPa can be described as follows. During the steady creep process, due to the softening of the material at high temperature, the strain rate is large, and the plastic deformation is large. After the transition to the accelerated creep process, the strain rate increases. Due to the different volume fractions of the primary γ' phase in the matrix, the fracture behavior of group B is hindered by the primary γ' phase at the grain boundary during the accelerated creep process, but the deformation continues. This is the reason why the elongation and reduction in area of group B are significantly higher than those of other groups. However, due to the low-volume fraction of the primary γ' phase, the material in group D was unstable and fractured during the transition to the accelerated creep stage. For the creep at 680 °C/830 MPa, the dislocation motion is blocked due to the lower temperature, but the different proportion of the primary γ' phase leads to the different creep process of different samples under this condition. The volume fraction of the group A sample is larger, and the grain deforms to the pinning effect, so there is almost no deformation in the steady-state creep process, or the deformation rate is extremely slow, and it is difficult to transition to the accelerated creep process in the creep process, so the creep life is the longest. For group C, the temperature is low in the creep process, there is no primary γ' phase pinning grain boundary, and there is no softening effect of high temperature in the creep process. In the creep process, it shows low elongation and low rupture life.

5. Conclusions

- (1) The specimens with different volume fractions of the primary γ' phase have an obvious effect on the high-temperature rupture properties, and the rupture life of the primary γ' phase with high-volume fraction is longer. The material exhibits better plasticity at 760 °C.
- (2) The high-volume-fraction primary γ' phase sample shows transgranular fracture during the fracture process, and the low-volume-fraction γ' phase sample is more inclined to intergranular fracture.
- (3) During the long-term aging process, the secondary γ' phase in the crystal will also change. With the extension of time, the secondary γ' phase tends to be more evenly distributed.
- (4) The primary γ' phase can hinder transgranular fracture and intergranular fracture, and the primary γ' phase can organize dislocations to migrate to grain boundaries, which is more obvious in high-volume-fraction samples.

Author Contributions: Data curation, Y.X., J.L., S.H. and W.Z.; writing—original draft, X.Z.; writing—review and editing, R.D.; supervision, T.X. All authors have read and agreed to the published version of the manuscript.

Funding: This research was funded by the Inner Mongolia Autonomous Region Science and Technology Plan Project, grant number 2021GG0266, and the Inner Mongolia University of Technology 2022 Science and Technology Innovation Fund for Undergraduates, grant number 88.

Data Availability Statement: Data are contained within the article.

Acknowledgments: Thanks to the experimental materials provided by Baowu Special Metallurgical Company and thanks to the Inner Mongolia Autonomous Region Science and Technology Plan Project for providing financial support for this experiment.

Conflicts of Interest: The authors declare no conflicts of interest.

References

1. Du, J.H.; Qu, J.L.; Deng, Q.; Zhuang, J.Y.; Liu, Q.B.; Lu, C.F.; Chen, G.S. As-Cast Microstructure and Homogenization Process of Alloy GH720Li. *J. Iron Steel Res.* **2005**, *17*, 60–64.
2. Qu, J.L.; Yi, C.S.; Chen, J.W.; Shi, Y.T.; Bi, Z.N.; Du, J.H. Research progress of precipitated phase in GH4720Li superalloy. *J. Mater. Eng.* **2020**, *48*, 73–83.
3. Zhang, R.; Liu, P.; Cui, C.; Qu, J.; Zhang, B.; Du, J.; Zhou, Y.; Sun, X. Present Research Situation and Prospect of Hot Working of Cast & Wrought Superalloys for Aero-Engine Turbine Disk in China. *Acta Metall. Sin.* **2021**, *57*, 1215–1228.
4. Meng, L.S.; Duan, F.Z.; An, T. Effects of γ/γ' eutectic on corrosion resistance of GH4720Li superalloy. *China Metall.* **2020**, *30*, 35–40.
5. Jackson, M.; Reed, R. Heat treatment of UDIMET 720Li: The effect of microstructure on properties. *Mater. Sci. Eng. A* **1999**, *259*, 85–97. [[CrossRef](#)]
6. Ning, Y.; Wang, T.; Fu, M.; Li, M.; Wang, L.; Zhao, C. Competition between work-hardening effect and dynamic-softening behavior for processing as-cast GH4720Li superalloys with original dendrite microstructure during moderate-speed hot compression. *Mater. Sci. Eng. A* **2015**, *642*, 187–193. [[CrossRef](#)]
7. Kozar, R.; Suzuki, A.; Milligan, W.; Schirra, J.; Savage, M.; Pollock, T. Strengthening Mechanisms in Polycrystalline Multimodal Nickel-Base Superalloys. *Met. Mater. Trans. A* **2009**, *40*, 1588–1603. [[CrossRef](#)]
8. Grant, B.M.; Francis, E.M.; da Fonseca, J.Q.; Daymond, M.R.; Preuss, M. Deformation behaviour of an advanced nickel-based superalloy studied by neutron diffraction and electron microscopy. *Acta Mater.* **2012**, *60*, 6829–6841. [[CrossRef](#)]
9. Zhang, P.; Yuan, Y.; Gu, Y.; Yan, J.; Dang, Y.; Lu, J.; Wang, J. Investigation on the tensile deformation mechanisms in a new Ni-Fe-base superalloy HT700T at 750 °C. *J. Alloys Compd.* **2020**, *825*, 154012. [[CrossRef](#)]
10. Zhou, H.; Chang, H.; Feng, Q. Transient minimum creep of a γ' strengthened Co-base single-crystal superalloy at 900 °C. *Scr. Mater.* **2017**, *135*, 84–87. [[CrossRef](#)]
11. Zhu, J.Q.; An, C.X.; Lu, Y.X. Research Progress on Effect of γ' Phase on Strength, Fatigue and Creep Properties of Nickel-Based Superalloys. *Mater. Mech. Eng.* **2023**, *47*, 71. [[CrossRef](#)]
12. Zhang, H.; Li, Y.; Ma, T.; Chang, T.; Zhang, P.; Fang, X.; Huang, K. Tailoring of nanoscale γ' precipitates and unveiling their strengthening mechanisms in multimodal nickel-based superalloy GH4720Li. *Mater. Charact.* **2022**, *188*, 111918. [[CrossRef](#)]
13. Singh, J.; Verma, A.; Khan, S.; Thota, M. Delineating hardening contributions of secondary and tertiary γ' particles in an aged Alloy 693. *Mater. Sci. Eng. A* **2020**, *785*, 139384. [[CrossRef](#)]
14. Zhao, P.F.; Hou, K.L.; Wang, M.; Ou, M.Q.; Yang, Y.Q.; Ma, Y.C. Effects of sub-solvus ageing on the tensile and creep properties of a new cast nick-el-based superalloy. *J. Mater. Sci. Technol.* **2025**, *212*, 289–302. [[CrossRef](#)]
15. Yu, B.; Wang, T.; Wei, L.; Jiang, S.; Zhang, H. Effect of aging time on precipitates and mechanical properties of the electron beam freeform fabricated Ni-Fe-Cr alloys reinforced by γ' and TiC phases. *Mater. Charact.* **2024**, *214*, 114118. [[CrossRef](#)]
16. Wang, Z.; Ning, Y.; Huang, S.; Di, P.; Liu, Q. Effect of μ precipitation and γ' evolution on intra-/intergranular strength of Ni-Co-Cr-based superalloys after 800 °C thermal exposure. *J. Alloys Compd.* **2024**, *999*, 175073. [[CrossRef](#)]
17. Galizoni, B.B.; Couto, A.A.; Reis, D.A.P. Heat Treatments Effects on Nickel-Based Superalloy Inconel 713C. *Metals* **2019**, *9*, 47. [[CrossRef](#)]
18. Wei, Z.; Jingnan, L.; Ruifeng, D.; Zishuai, C.; Jian, L.; Xing, Z.; Qingzeng, W.; Jinglong, Q. Effect of heat treatment process parameters on the microstructure and properties of GH4720Li superalloy. *Mater. Res. Express* **2023**, *10*, 016514. [[CrossRef](#)]
19. Song, K.Y.; Li, Y.S.; Sun, Y. Effect of Precipitates Characteristics on Fatigue Properties of GH4720Li Alloy. *Rare Met. Mater. Eng.* **2023**, *52*, 2851–2858.
20. Tang, C.; Cheng, S.J.; Qu, J.L. Effects of Mixed-Grain Microstructure on High Temperature Mechanical Properties of GH4720Li Alloy. *Rare Met. Mater. Eng.* **2021**, *50*, 3280–3287.
21. Zhang, S. Research of morphology evolution of precipitation during aging and the effects of precipitation on creep property of 617B superalloy. In Proceedings of the IOP Conference Series-Earth and Environmental Science, Harbin, China, 29 November–1 December 2019.
22. Tsai, Y.-L.; Wang, S.-F.; Bor, H.-Y.; Hsu, Y.-F. Effects of alloy elements on microstructure and creep properties of fine-grained nickel-based superalloys at moderate temperatures. *Mater. Sci. Eng. A* **2013**, *571*, 155–160. [[CrossRef](#)]
23. Zhang, Z.; Ding, R.; Guo, Q.; Liu, C.; Liu, Y. Improving the microstructural stability and tensile properties of Inconel 617 superalloy at high temperature by stabilization of the γ' phase. *J. Mater. Res. Technol.* **2024**, *29*, 2991–2998. [[CrossRef](#)]
24. Wei, L.; Pan, B.; Wang, Y.; Li, B.; Jia, X. Microstructure evolution and creep-rupture behaviour of a low-cost Fe-Ni-based superalloy. *Mater. Technol.* **2023**, *38*, 2270865. [[CrossRef](#)]
25. Kim, S.H.; Kim, H.; Kim, N.J. Brittle intermetallic compound makes ultrastrong low-density steel with large ductility. *Nature* **2015**, *518*, 77–79. [[CrossRef](#)] [[PubMed](#)]
26. Sun, F.; Gu, Y.F.; Yan, J.B. Creep deformation and rupture mechanism of an advanced wrought Ni-Fe-based superalloy for 700 degrees C class A-USC steam turbine rotor application. *J. Alloys Compd.* **2016**, *687*, 389–401. [[CrossRef](#)]

27. Torfeh, M.; Mirbagheri, S.M.H.; Cormier, J.; Aghazadeh Mohandesi, J.; Nakhodchi, S. Intermediate temperature creep damage mechanisms of a directionally solidified Ni-based superalloy. *Mater. High Temp.* **2022**, *39*, 193–205. [[CrossRef](#)]
28. Wu, J.J.; Zhao, G.D.; Jiang, H.Y. Effect of Heating Process on γ' Dissolution and Grain Growth Behavior of Hard-Deformed Superalloy U720Li. *Rare Met. Mater. Eng.* **2024**, *53*, 2205–2216.

Disclaimer/Publisher's Note: The statements, opinions and data contained in all publications are solely those of the individual author(s) and contributor(s) and not of MDPI and/or the editor(s). MDPI and/or the editor(s) disclaim responsibility for any injury to people or property resulting from any ideas, methods, instructions or products referred to in the content.